Fine Scale 3D Wind Field Observation With a Multistatic Equatorial Atmosphere Radar

Koji NISHIMURA, Eikoh GOTOH and Toru SATO

Graduate School of Informatics, Kyoto University, Kyoto, Japan

(Manuscript received 1 November 2005, in final form 12 March 2006)

Abstract

Radar observation is widely recognized as an essential technique to study the three-dimensional dynamics of the atmosphere with a high temporal resolution. Conventional monostatic radar with a single aperture or array, however, has rather limited spatial resolution. This is because this radar can only obtain the radial component of the wind velocity, and thus it must observe at least three spatially separate target volumes to estimate the three components of the wind vector. In this paper, a multistatic radar observation technique, which uses two receiver arrays together with a high-gain rapid scanning mesosphere-stratosphere-troposphere (MST) radar, is presented. Multistatic receiver arrays obtain non-radial components of the wind velocity; hence, the technique enables us to determine 3D wind velocity at each minimum resolution volume. Consequently, it eliminates estimation error caused by horizontal inhomogeneity of the wind field and improves spatial resolution. Applying this technique, we made a series of tropospheric observations in September 2004, utilizing a newly developed digital receiver system at the Equatorial Atmosphere Radar, West Sumatra, Indonesia. Each receiver antenna is equipped with this digital receiver and recording system, which is constructed with a cost-effective ready-made digital receiver PCI board and a PC. This structure enables us to swing the receiving beam after an observation using digital beamforming techniques. First, the importance and the effectiveness of ground clutter rejection using an adaptive spatial filter, which is another advantage of digital receiver systems, is demonstrated. Then for the first time an example profile of a 3D wind velocity field with 1-km horizontal resolution at 3.8 km altitude is presented. Considering the accuracy of the multistatic radar system, the resulting wind field shows the existence of significant perturbation that previously would have been averaged in conventional monostatic radar observations.

1. Introduction

Owing to its exceptional capability for 3D wind velocity measurement, radar observation is essential in studies of the dynamical system of the atmosphere. Of all the atmospheric radars utilized, including the widely distributed mesosphere-stratosphere-troposphere (MST) radar network such as Jicamarca radar (Woodman and Guillen 1974), MU radar (Fukao et al. 1985) as well as the Equatorial Atmosphere Radar (EAR) (Fukao et al. 2003), monostatic radar systems are the type that have consistently been employed. A monostatic system is superior from the points of view of sensitivity, maintainability and economics, because it has a single large aperture antenna or array. On the other hand, from the point of view of spatial resolution, its function is fairly restricted because a monostatic radar system requires an assumption of homogeneity of the wind field, and thus it mainly provides a vertical profile of the wind velocity and turbulence intensity. This is because monostatic radar can only observe the radial components of the wind field, and that a 3D wind velocity needs to be esti-

Corresponding authors: Koji Nishimura and Toru Sato, Graduate School of Informatics, Kyoto University, Kyoto 606-8501, Japan.
E-mail: knish@ieee.org, tsato@kuee.kyoto-u.ac.jp

mated from several radial velocities of horizontally separate target volumes.

Spaced Antenna (SA) method (Röttger and Vincent 1978) is a scheme that does not require an assumption of horizontal homogeneity, and has been mainly used to measure horizontal components of wind velocity. However, the SA method requires an assumption of little or no vertical motion of the atmosphere and therefore it is not appropriate for tropical atmosphere measurements.

The tropical Pacific region especially the Indonesian Archipelago, in which the EAR is located, is considered a major source of global atmospheric circulation. The convection generated in this region is considered to be essential for this energy flow through the process that is currently being examined by a program called "Coupling Processes in the Equatorial Atmosphere (CPEA)" (Fukao 2006). Compared to a layered motion of the atmosphere, however, a convective motion, which is accompanied by turbulence, shows remarkably complex structure with changes in its momentum vectors. The restrictive resolution of a monostatic radar system imposes potential limitations in measuring the spatial scale of convective motions.

Multistatic radar is a progressive modification of monostatic radar that is ideally suited for high-gain MST radars. This system is equipped with multiple receiver arrays to simultaneously observe obliquely scattered echoes from a single target volume, together with the main radar. Hence it is possible to determine 3D velocity vectors in every single target volume as discussed in section 2. Figure 1 shows an outline of the differences between monostatic and multistatic radars. The multistatic radar can determine 3D wind velocities at each resolution volume while the monostatic radar can only observe one at each altitude.

In contrast to these advantages, there are several technical issues to be dealt with such as synchronization and maintainability to realize a practical multistatic radar. Historically, multistatic atmospheric radar, including bistatic radar, has mainly been employed for the study of the ionosphere with large incoherent scatter radars such as at the St. Santin (Amayenc et al. 1973) and EISCAT (Alcayde et al. 1982) facilities. In the neutral atmosphere

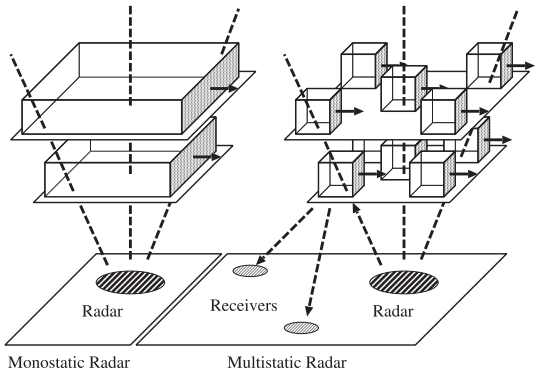

Fig. 1. Concepts of monostatic radar and multistatic radar. Each cubic cell shows a unit volume in which a 3D wind velocity can be determined.

region, Doviak et al. (1972) and Woodman (1980) succeeded in obtaining preliminary results of tropospheric and stratospheric observations using a S-band non-Doppler bistatic receiver aimed to enhance its layered scattering structure. Wurman et al. (1993) developed a bistatic and dual-monostatic S-band Doppler weather radar and showed comparable wind fields measured by both schemes. In these observations, however, strong clutters caused by the low-gain broad beam of the receiver appeared. For our observations, as the signal-to-noise ratio is severe, this clutter is a vital issue that needs to be addressed.

The current study is thus the first attempt to measure the 3D wind velocity with a multistatic system adapted to a giant atmospheric radar. In this study, the transmitter antenna beam direction is steered in the zenith angle region of 30°s. In traditional multistatic radars, the transmitter beam direction has been fixed, because it is difficult to simultaneously match the receiving beam direction to the target volume illuminated by the transmitter beam at multiple heights when the transmitter beam direction is altered. This problem is resolved by the use of post beam steering with digital receiver arrays, as described in section 2.

In the following sections, we first briefly examine the principles of wind velocity measurement with a multistatic radar system, focusing on a quantitative assessment of its accuracy. We next describe the system configuration, observational setups and data processing

schemes, which include adaptive clutter rejection. We finally present some examples of wind velocity fields obtained by the first series of experiments that took place in September 2004.

2. Principle of multistatic radar and its estimation error

2.1 Principle

Being different from conventional monostatic systems, multistatic radar has multiple receiver sets to simultaneously observe an echo from a target at separate places. The principle of multistatic radar is illustrated (note that a bistatic subsystem is illustrated) in Fig. 2. Hereafter, a *multistatic* is referred to as being one accompanied with at least two receiver arrays, and a *bistatic* as one with one receiver array.

Let $\boldsymbol{e}_0$ be a normalized direction vector toward the target from the radar, and $\boldsymbol{e}_i$ be that from the i-th receiver ($i = 1, 2$). The Doppler velocity, measured from the backscattering of the target (denoted v_0) is described as,

$$v_0 = \boldsymbol{e}_0^t \boldsymbol{v}_{\text{target}}, \tag{1}$$

where $\boldsymbol{v}_{\text{target}}$ is the true wind velocity vector.

Doppler velocities v_i measured by the bistatic subsystems have a different nature, described as,

$$v_i = \frac{1}{2}(\boldsymbol{e}_0 + \boldsymbol{e}_i)^t \boldsymbol{v}_{\text{target}}. \quad (i = 1, 2) \tag{2}$$

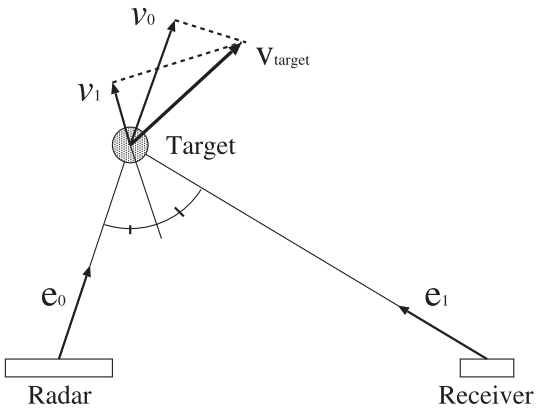

Fig. 2. Measurement principles in a multistatic atmospheric radar system. Note that a bistatic subsystem is illustrated. The line-of-sight Doppler velocities measured by the radar and the receiver correspond to $\boldsymbol{v_0}$ and $\boldsymbol{v_1}$, respectively.

When we have two additional receiver arrays, we can estimate $\boldsymbol{v}_{\text{target}}$ as,

$$\boldsymbol{v}_{\text{target}} = \begin{pmatrix} \boldsymbol{e}_0^t \\ \frac{\boldsymbol{e}_0^t + \boldsymbol{e}_1^t}{2} \\ \frac{\boldsymbol{e}_0^t + \boldsymbol{e}_2^t}{2} \end{pmatrix}^{-1} \begin{pmatrix} v_0 \\ v_1 \\ v_2 \end{pmatrix}. \tag{3}$$

2.2 Estimation error

Estimation error of the resulting 3D wind velocity depends on the estimation errors σ_0, σ_1 and σ_2 of v_0, v_1 and v_2, respectively, and the angles between $\boldsymbol{e}_0$, $\boldsymbol{e}_1$ and $\boldsymbol{e}_2$. Let ε_u, ε_v and ε_w be the estimation errors of zonal (u), meridional (v) and vertical (w) components of the wind vector $\boldsymbol{v}_{\text{target}}$, the error variance is described as, (Wurman et al. 1993)

$$\begin{pmatrix} \varepsilon_u^2 \\ \varepsilon_v^2 \\ \varepsilon_w^2 \end{pmatrix} = \begin{pmatrix} \alpha_{11}^2 & \alpha_{12}^2 & \alpha_{13}^2 \\ \alpha_{21}^2 & \alpha_{22}^2 & \alpha_{23}^2 \\ \alpha_{31}^2 & \alpha_{32}^2 & \alpha_{33}^2 \end{pmatrix} \begin{pmatrix} \sigma_0^2 \\ \sigma_1^2 \\ \sigma_2^2 \end{pmatrix} \tag{4}$$

where

$$\begin{pmatrix} \alpha_{11} & \alpha_{12} & \alpha_{13} \\ \alpha_{21} & \alpha_{22} & \alpha_{23} \\ \alpha_{31} & \alpha_{32} & \alpha_{33} \end{pmatrix} = \begin{pmatrix} \boldsymbol{e}_0^t \\ \frac{\boldsymbol{e}_0^t + \boldsymbol{e}_1^t}{2} \\ \frac{\boldsymbol{e}_0^t + \boldsymbol{e}_2^t}{2} \end{pmatrix}^{-1}. \tag{5}$$

The signal of atmospheric echo is a stochastic process whose power spectrum is well approximated by a Gaussian distribution with a standard deviation of σ_r, and the fluctuation is proportional to its power spectral density. In a real analysis, an incoherent integration or a smoothing of the spectra is necessary for an accurate estimation of the Doppler shift.

Estimation error of the radial Doppler velocity, measured with each receiver array, is described by spectral resolution δ_f, spectral width of the signal σ_r and the number of incoherent integration N as follows:

$$E = k\sqrt{\frac{\lambda \sigma_r \delta_f}{2N}} \tag{6}$$

where λ is the wave length of the radio that is 6.38 m and k is a constant characteristic of an estimation method. According to Yamamoto et al. (1988), the constant k is 0.38 and 0.63 for the moment and the fitting methods, respectively.

In this study, to determine the radial velocity, we used a fitting of a parabolic function in a log-scale spectrum and also manual correc-

tions in some part. Therefore, it is rather unclear which k is best to chose. Erring on the side of safety, we chose the larger constant $k = 0.63$ for our entire fitting process. In our data processing process, we divide a single period of 81.6 s into eight 10.2 s subsections for the Doppler-spectral calculation. Substituting $\lambda = 6.38$ m, $N = 8$, $\delta_f = 0.098$ Hz, and $\sigma_r = 0.7$ ms^{-1} which is typical for tropospheric observations, into eq. (6), we obtain $E = 0.104$ ms^{-1}.

2.3 *Receiver locations*

In a multistatic system, the estimation error of 3D wind velocity is evaluated by the estimation errors σ_0, σ_1 and σ_2, into v_i of eq. (4). For examining the location of receivers, we first evaluate the estimation error of 2D wind velocity in a bistatic system model. For observation with a vertical beam from the radar, the estimation error of the vertical component is given by

$$\varepsilon_w^2 = \langle (w - \tilde{w})^2 \rangle = E^2, \tag{7}$$

where $\tilde{w}$ is an estimate of the vertical component w, and that of horizontal component u is expressed as

$$\varepsilon_u^2 = \langle (u - \tilde{u})^2 \rangle = \frac{1}{b^2}(6h^2 + 2h\sqrt{h^2 + b^2} + 5b^2)E^2, \tag{8}$$

where $\tilde{u}$ is an estimate of u, h is the altitude of the target volume, and b is the length of the base line between the radar and the receiver, respectively.

Baselines affect the estimation accuracy of 3D wind velocity; a longer length effectively provides a higher accuracy. Figure 3 shows the curve of ε_u versus b. However, we have a height ceiling for sensitivity that depends on the number of antennas. The profile of signal-to-noise ratio (SNR) measured by the EAR, which is equivalent to a receiver consisting of 560 antennas, is shown in Fig. 4. In this observation, each multistatic receiver consists of 10 antennas; Therefore, the SNR profile is shifted -17.5 dB ($= 10/560$) from that in Fig. 4. Since the detection limit of atmospheric echo is around -15 dB in SNR, the height ceiling for sensitivity reaches 8 km.

Considering the accuracy effect and the height ceiling for sensitivity, we chose two suitable places that are approximately 1300 m away to the west and the south of the EAR, respectively. Within the lower than 8 km altitude limit for sensitivity, these two positions give an estimation error of better than 2 ms^{-1} for the horizontal wind components. The relative position of the two places to the EAR is

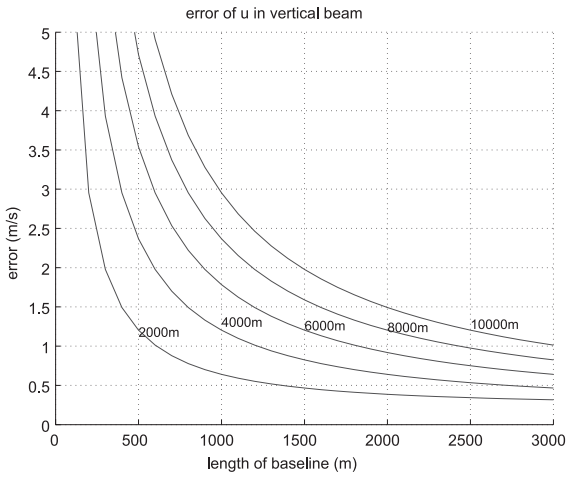

Fig. 3. Estimation error of the horizontal wind velocity in a vertical beam versus the length of the baseline.

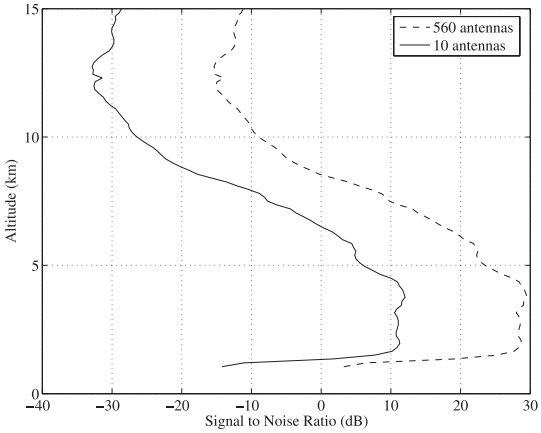

Fig. 4. Signal-to-noise ratio profile measured by the EAR in a monostatic observation using Spano code (dashed). The solid line shows an SNR which is shifted by -17.5 dB ($= 10 \log_{10}(560/10)$) from the dashed line assuming 10 antennas are used in a receiver site.

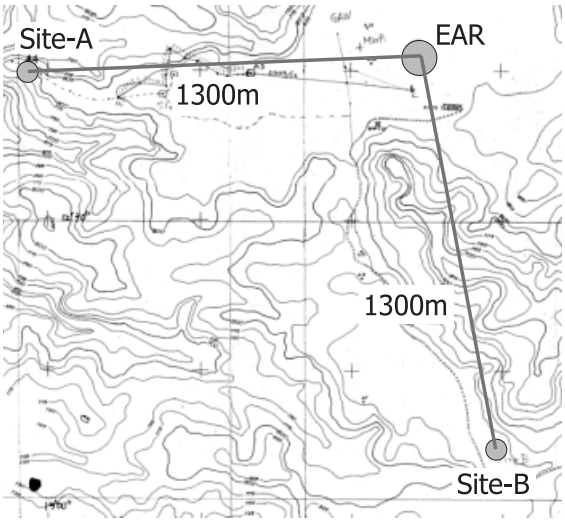

Fig. 5. A plan view of the EAR, site-A and B.

Table 1. System parameters for digital receivers.

Antenna	4-element Yagi
Bandpass Filter	
Band Width	10 MHz
Pre-Amplifier	
Gain	25 dB
Noise Figure	<2 dB
AD Converter	
Analog Input	2 channels
Resolution	14 bits
Maximum Allowed Input	+10 dBm
Sample Rate	64 MHz
Digital Down Converter	
Conversion Rate	1/32
Recording	
Coherent Integration	30 times
Resolution	32 bits
Sample Rate	2 MHz

$(-1278, -6, -57)$ and $(306, -1296, 15)$, respectively, in (x, y, z) coordinates (in meters). Hereafter, these two sites for the receiver arrays (see Fig. 5) are referred to as Site-A (west) and Site-B (south).

3. Observational equipment

Atmospheric radar needs to have a very wide dynamic range covering from galactic noise to ground clutter. In the frequency band of 47 MHz, which is used by the EAR, the largest noise source is galactic radiation that has an average temperature T_g roughly represented by 7500 K. The power of galactic noise is given by

$$P = k_B T_g B \tag{9}$$

$$= 1.05 \times 10^{-9}\ \mathrm{mW}, \tag{10}$$

where k_B is the Boltzmann constant and B is the bandwidth of the receiver, which is 10 MHz in this study. Maximum transmission loss caused by cables and connectors is estimated to be 3 dB; Therefore, galactic noise at the output of antenna is approximately −93 dBm where 0 dBm is equal to 1 mW. The digital receiver has analog-to-digital (A/D) converters with resolution of 14 bits, which corresponds to the dynamic range of 84 dB, and the maximum input level of +10 dBm.

The average power of quantization noise is approximately 11 dB lower than the minimum quantization scale. To avoid losing the SNR in the atmospheric echo, the input galactic noise level should be sufficiently higher than the quantization noise level. Thus we set the gain of pre-amplifier to 25 dB which increases the galactic noise to −75 dBm. Related parameters are shown in Table 1.

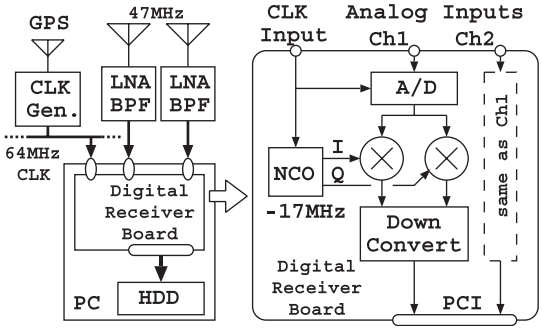

Fig. 6. Schematic diagram of a digital receiver board and the entire digital receiver system.

In general, digital receiver systems with full adaptive capability for radar are quite expensive. For this type of observation we developed a simple and highly cost-effective digital receiver system using PCs, and Echotek ECDR-214PCI PCI boards with A/D converters and digital down converters on-board. Figure 6 is

the schematic diagram of the system. The PCI board has two analog inputs, A/D converters and four independent signal processing units. Hence each board is used as two receiver systems with I/Q channels. Each receiver system consists of an antenna, a band-pass filter with a band width of 10 MHz and a low noise amplifier with a gain of approximately 25 dB, followed by the board.

The sampling clock is generated by a GPS receiver system with a reference clock output of 10 MHz followed by a digital direct synthesizer (DDS) that up-converts the clock signal to 64 MHz. The 47 MHz RF signal received by the antenna is directly sampled and quantized by the A/D converter on-board at this clock frequency with a resolution of 14 bits. The digitized signal is filtered and down-converted to the baseband with a band width of 2 MHz by three stage CIC and FIR filters, and a down-sampler in a 4-channel digital down-converter (DDC) chip on the ECDR-214PCI board.

Both Site-A (west) and Site-B (south) receiver sites consist of 10 antennas that are aligned roughly in a triangular form with an interval of 0.7λ (≈ 4.5 m) that theoretically has optimal sidelobe suppression.

4. Observational scheme

Observations were made from 25 through 29th September 2004. Observational modes of the EAR are shown in Table 2. The modes were altered in order from A to C every 82 seconds. The Mode-A is aimed for tropospheric observations that utilize a short pulse of 1 μsec. Modes-B and -C are mainly aimed for stratospheric observations that make use of longer pulses of 16 μsec, which have a gain of 16 times as much as that of Mode-A. In every mode, the direction of the transmitting beam changes in a pulse to pulse manner in the order shown in Table 2.

The observational scheme differs between the monostatic EAR and the multistatic receivers. For the monostatic EAR, received signals are sampled and quantized at the rate of 1 MHz after de-modulation. A pulse compression process of a complementary code pair follows only for Modes-B and -C. Signals are further coherently averaged at the interval of the IPP $\times$ the number of beam directions ($= 5$), which corresponds to 1, 2 and 2 msec for Modes-A, -B and -C, respectively, prior to being stored on HDDs.

Table 2. Observational modes of EAR. (IPP: Inter-Pulse Period, PL: Pulse Length, SPL: Sub-Pulse Length, NCOH: Number of Coherent Integration, NICOH: Number of Incoherent Integration, NFFT: FFT data length)

Mode	Target	IPP (μs)	SPL (μs)	PL (μs)
A	Troposphere	200	1	1
B	Stratosphere	400	1	16
C	Stratosphere	400	1	16

Mode	NCOH	NICOH	NFFT	Compression
A	64	5	256	no
B	32	5	256	complementary
C	32	5	256	complementary

Mode	Beam Directions (Azimuth, Zenith Angle)				
A	(0, 0)	(45, 30)	(135, 30)	(225, 30)	(315, 30)
B	(0, 0)	(0, 30)	(90, 30)	(180, 30)	(270, 30)
C	(0, 0)	(0, 10)	(90, 10)	(180, 10)	(270, 10)

For the multistatic receivers, received signals are oversampled and quantized at a rate of 2 MHz via on-board down-converters. After being transferred into the memory of a PC via a PCI bus, the 16-bit digitized signal is coherently averaged for 30 times at intervals of 1 msec, then stored on HDDs. This interval of 1 msec is equivalent to the IPP $\times$ the number of beam directions of Mode-A. The pulse compression processes could not be employed in real-time because the absolute time of the multistatic receivers was not fully synchronized to that of the EAR.

5. Post-observational signal processing

The procedure for post-observation signal processing to derive an altitude-velocity spectrum from the received signals is as follows. All the signals are first divided into samples in a range-by-range manner at each beam direction. Second, to gain the SNR, the phase of the signal of each antenna is rotated to match the relative phase angle considering a plane wave from the corresponding target volume. Here, let $\boldsymbol{d}_n$ be the relative displacement of the n-th antenna; thus the relative phase rotation of an echo is derived as,

$$\phi_n = \boldsymbol{k} \cdot \boldsymbol{d}_n \tag{11}$$

where $\boldsymbol{k}$ is the wave number of the echo from a target volume. This process is equivalent to what is called post beam steering, in which the desired direction of the plane wave is different depending on not only the transmitted beam direction, but also the observation height.

Third, taking advantage of independently recorded signals for every antenna, ground clutter is eliminated using an adaptive spatial filtering technique (Kamio et al. 2004; Cheong et al. 2006). This process is especially important for multistatic observations, because each multistatic receiver array consists of only 10 antennas and thus its sidelobe level is approximately 15 dB higher than that of the monostatic EAR. This sidelobe level is not sufficiently low to suppress ground clutter, resulting in a serious contamination from clutter in the atmospheric echo. To provide an accurate estimate of wind velocity, we employed an adaptive signal processing technique that forms a spatial filter to eliminate ground clutter.

The procedure is described as the problem of finding optimal weights which are used in the weighted sum of signals received at the antennas which make up a receiver array. $\boldsymbol{x}$ denotes a set of signals associated with the n-th antenna as

$$\boldsymbol{x}(i) = (x_1(i), x_2(i), \ldots, x_N(i))^t, \tag{12}$$

and thus $\boldsymbol{w}$ a set of weights for summation as

$$\boldsymbol{w} = (w_1, w_2, \ldots, w_N)^t. \tag{13}$$

The optimal weight vector is given as a solution that minimizes the resulting average power

$$P = \boldsymbol{w}^H R \boldsymbol{w} \tag{14}$$

where R is an averaged covariance matrix given by

$$R = \begin{pmatrix} \Sigma x_1(i)x_1^H(i) & \Sigma x_1(i)x_2^H(i) & \cdots & \Sigma x_1(i)x_N^H(i) \\ \Sigma x_2(i)x_1^H(i) & \Sigma x_2(i)x_2^H(i) & \cdots & \Sigma x_2(i)x_N^H(i) \\ \vdots & \vdots & \cdots & \vdots \\ \Sigma x_N(i)x_1^H(i) & \Sigma x_N(i)x_2^H(i) & \cdots & \Sigma x_N(i)x_N^H(i) \end{pmatrix} \tag{15}$$

under the condition of constant gain to waves coming from the target volume, which is given by

$$\boldsymbol{c}^H \boldsymbol{w} = 1, \tag{16}$$

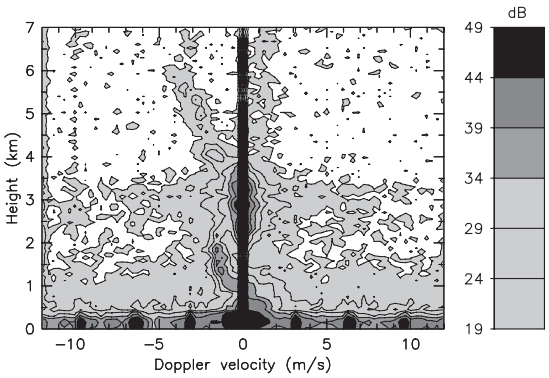

Fig. 7. An altitude-velocity spectrum observed at site-B at 12:00 LT 26, Sep, 2004, in mode-A for the direction $(225, 30)$, after a coherent sum of 8 antennas out of 10. (For reasons of the stability of the equipment, only 8 antennas worked at this period.)

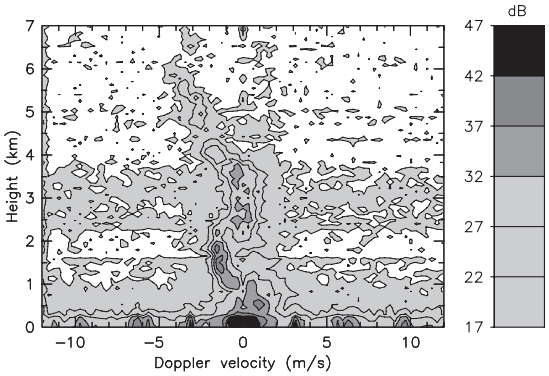

Fig. 8. The same as 7 but with the adaptive spatial filtering procedure.

where

$$\boldsymbol{c} = (e^{-i\phi_1}, e^{-i\phi_2}, \ldots, e^{-i\phi_N})^t. \tag{17}$$

The optimal weight $\boldsymbol{w}_{\mathrm{opt}}$ is given by

$$\boldsymbol{w}_{\mathrm{opt}} = \frac{R^{-1}\boldsymbol{c}}{\boldsymbol{c}^H R^{-1} \boldsymbol{c}}. \tag{18}$$

Figure 7 and Fig. 8 show altitude-velocity spectra before and after, respectively, the adaptive clutter suppression process. A strong ground clutter component, which is dominant at and around the zero Doppler component in Fig. 7 is almost completely suppressed in Fig. 8. It should be noted that the atmospheric echo com-

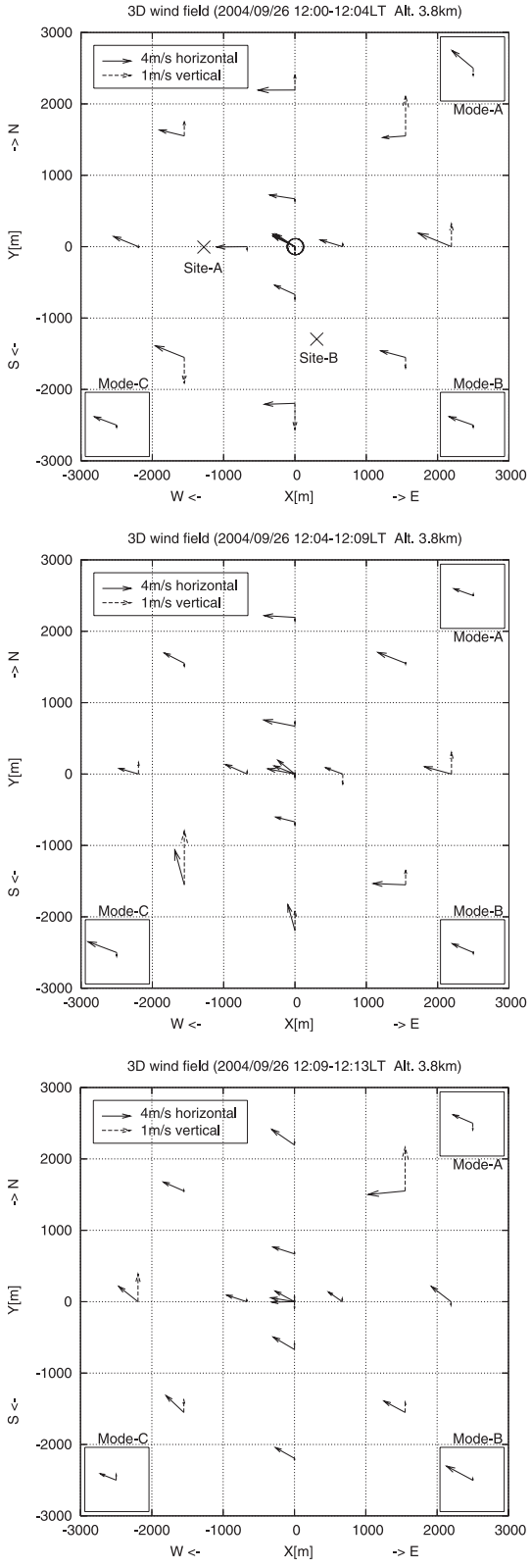

ponents with zero Doppler frequency seen at 2.5–3.5 km height are conserved in this processing. There is a slight depression of the SNR as seen in the echoes at 6–7 km, which is the side effect of controlling the phase of individual antenna elements.

Doppler velocity is, basically, estimated by fitting the Gaussian function to a spectrum around the peak of the echo. This procedure is done by fitting a parabolic function in a logarithmic scale to the spectral peak and an adjacent component on each side. It should be noted that the Doppler velocity in some data used in this paper are corrected manually to eliminate an obvious misestimate with this algorithm.

6. Resulting 3D wind field

During the observation from 25 through 29th September 2004, of over 100 hours of data were obtained. Because of its huge size, analyses of the entire data set are still under way. It is also beyond the scope of this paper to study in detail the fine scale wind velocity field. Here we only show preliminary examples of the 3-D wind velocity field to demonstrate the capability of the multistatic radar system.

By combining the three observational modes, A–C, listed in Table 2, 15 horizontal locations are sampled at each height with a time resolution of about 4 minutes. Figure 9 shows an example of the 3-D wind velocity field thus obtained for three consecutive observation cycles at a height of 3.8 km. Three arrows in the insets at the corners of each figure denote the wind velocity vectors determined by the monostatic EAR. The solid arrows show the horizontal wind velocity components, and the dashed arrows show the vertical component.

The three arrows starting from the origin represent the three estimates with Modes A,

Fig. 9. Example of a horizontal section of the wind velocity field at three consecutive observation cycles. The origin of each arrow is the center of the target volume. The arrow with solid line shows a 2D horizontal velocity vector (u,v), and that with a dashed line shows a vertical component w. In the top panel, two crosses are placed at the receiver sites.

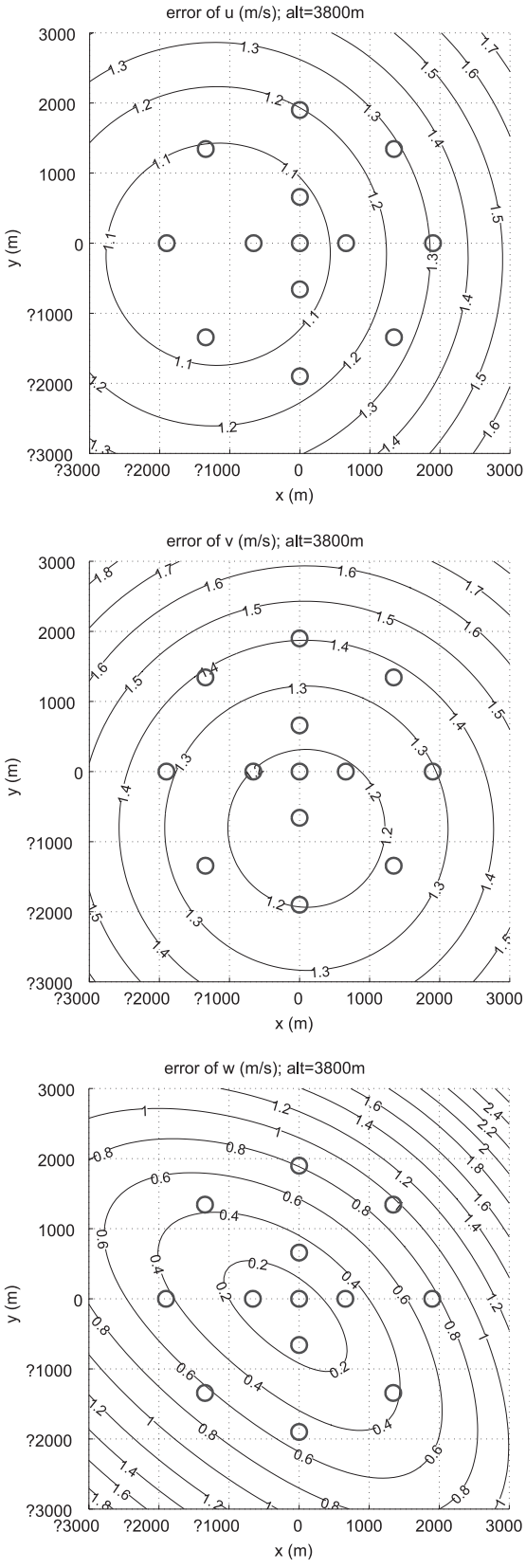

B, and C, all of which include this location. The differences among these arrows indicate temporal variations of the wind velocity over the observation cycle of 4 minutes, as well as the random errors. It should be noted that the vertical component is magnified by 4 times compared to the horizontal component. As the beam width of 3.4° corresponds to the horizontal resolution of 240 m at this height, the wind velocity field may be under-sampled especially at around the 8 locations on the outer circle.

The height of 3.8 km is chosen because the echo power profile shows a clear peak at this altitude, and thus the problem of range sidelobes can be eliminated in Modes B and C of Table 2. While, in principle, the pulse compression scheme of the 16-element complementary codes used in these modes has no range sidelobe, we mistakenly averaged the echoes of the complementary pulse pair in the real-time signal processing before the pulse compression. The two sequences that constitute the complementary codes have the same pattern for the first 8 elements, and the same pattern with the opposite sign for the latter 8 elements. As a result, the pulse compression turned into an 8-element binary code with a fairly high range sidelobe level after the averaging.

Since Mode A employs a single pulse, there is no problem regarding the range sidelobe. Instead, the signal-to-noise ratio of Mode A is 9 dB lower than those of Modes B and C. The estimation error of the wind velocity at the directions measured with Mode A, which are at the diagonal locations in Fig. 9, is thus larger than those of the other locations measured with Modes B and C.

The errors are for data with sufficiently high signal-to-noise ratios, which is the case for Modes B and C that are evaluated according to the discussion in section 2. Figure 10 shows the expected random errors of the three wind com-

Fig. 10. Estimation errors of u, v and w in a horizontal section at 3800 m in altitude. The estimation error of each radial velocity is assumed to be 0.104 ms^{-1}. The open circles indicate the targets and their size shows the one-way half-power area of the transmitted beams at this altitude.

ponents as a function of the observation point at a height of 3.8 km. The difference in the zonal and meridional components is due to the non-orthogonal alignment of the two baselines between the EAR and the receiver arrays. The error of the estimated zonal and meridional wind components is about 1.0 m/s at near the center of the illuminated area, and increases to about 1.4 m/s at the outer edge.

While the mean horizontal wind is consistently westward with a slight northward offset at all locations in the three observation cycles in Fig. 9, there is a substantial perturbation superimposed on the mean wind field even at the non-diagonal locations observed with Modes B and C. Although the magnitude of the perturbation falls within the limit of accuracy indicated by Fig. 10 at some locations, there are cases exceeding this limit such as a clear trend along the Y-axis from -2200 m toward $+2200$ m during 12:04–12:09 LT. It should be noted that large perturbations at diagonal locations observed with Mode A contain larger random errors than at other locations, and thus require further verification.

The error of the vertical wind component depends largely on the relative location of the observation point with respect to the baseline. While it is less than 0.2 m/s above the center of the baseline, the error increases rapidly as the distance increases, and exceeds 0.4 m/s when the point is above outside the baseline. In our current observations, the vertical wind component is most reliable at the locations in and around the fourth quadrant. The downward velocity of 1.0 m/s at the south point at 12:00–12:04, and the upward velocity of 0.9 m/s at the west point at 12:09–12:13 seem to be examples of real perturbations, which are most likely due to weak local convections. However, more careful verification is required to assess perturbations in the vertical component.

To further examine the significance of the perturbation wind field, we compared the vertical profiles of the wind field estimated by the proposed multistatic and by the monostatic methods using the EAR alone. Figure 11 shows the vertical profile of the two horizontal wind components observed by Modes-A, -B, and -C for the period of the middle panel of Fig. 9. The multistatic method is applied to the data of the vertical beam position, which is included in all

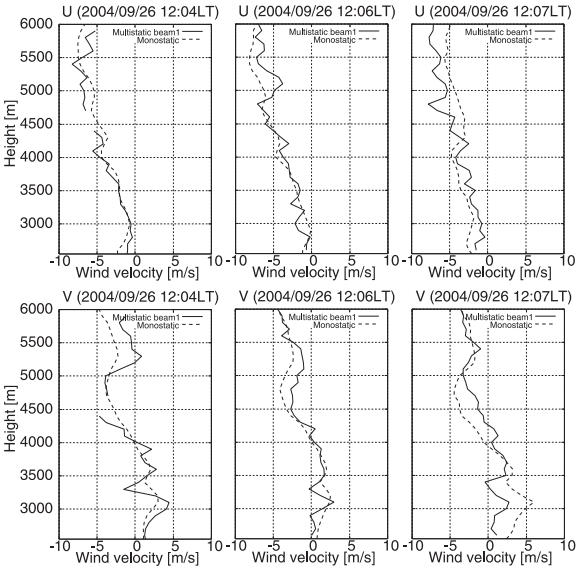

Fig. 11. Vertical profiles of the zonal (top row) and the meridional (bottom row) wind components estimated by the two observation methods. The solid line is by the monostatic method using the data of the EAR alone, and the dotted line is by the proposed multistatic method.

three modes. The solid line is the monostatic estimate assuming horizontal uniformness using the five beams observed by the EAR, and the dotted line is the multistatic estimate. It is clear from this figure that the wind profiles estimated by these two methods often show clear and persistent differences over a large height interval of more than 1 km. As the height resolution is 150 m, this persistent difference is clear evidence that these are due to horizontal inhomogeneity of the wind field, and not due to random errors in the estimates. This comparison suggests that instantaneous profiles observed by the DBS method with a monostatic radar may have an error of up to 3 m/s. The large vertical extent of this perturbation suggests that it is related to convective motions, but we need to avoid speculative discussions as no supporting meteorological data from during the observation period is available.

It should be noted that the profiles of 12:04 LT are taken by Mode-A, which has a significantly lower SNR because it uses a single pulse. The data with detectability of less than

3 is removed from the profile, which is the case for the data around heights of 4.5 km. On the other hand, data of 12:06 LT and 12:07 LT are processed with pulse compression of 8 bits. As described before, this mode may suffer from code sidelobes, and thus should be interpreted with care. If the echoes are contaminated with code sidelobes, the wind velocity estimate is biased to that of a different altitude, differing by up to 1.2 km from the center of the scattering volume. However, if a layer with a strong echo power affects neighboring heights, they would show the same wind velocity as that of the affecting layer, resulting in a constant velocity profile with height. The profiles shown here always show a clear and continuous trend with height, which is direct evidence that the code sidelobes do not have any significant effect in this case. Similar persistent difference between the two methods is also found in data of 12:04 LT, which is free from the problem of code sidelobe.

7. Summary

Preliminary results of the first multistatic radar observations of the tropospheric wind field are presented. The system consists of the existing Equatorial Atmosphere Radar, with two digital receiver arrays located at 1.3 km from the main antenna array. In the receiver arrays, data from individual antenna elements are recorded separately for post-observational signal processing, which include the coherent addition of signals at desired beam directions and heights. Adaptive clutter rejection is also performed at this stage, which demonstrated a very high capability for suppressing strong echoes from surrounding mountains. Finally, examples of the fine-scale distribution of a 3-D wind velocity field, which were obtained during the experiment which took place in September 2004, is presented as the first atmospheric radar investigation to study the velocity perturbations inside a volume of about 4-km diameter. Theoretical examination of the estimation error has revealed that significant perturbation components existed in the observed wind velocity field.

Acknowledgment

The authors thank Jeffrey Hagen (Arecibo Observatory) for providing the computer programs for the digital receiver. This study is supported by a Grant-in-Aid for Scientific Research on Priority Area-764 of the Ministry of Education, Culture, Sports, Science and Technology of Japan (Grant No. 13136205). This work is also supported in part by the 21st Century COE Program (Grant No. 14213201).

Appendix

Equation (7) and eq. (8)

Following the manner as in eq. (4), a bistatic system is described as

$$\begin{pmatrix} u \\ v \end{pmatrix} = \begin{pmatrix} \beta_{11} & \beta_{12} \\ \beta_{21} & \beta_{22} \end{pmatrix} \begin{pmatrix} v_0 \\ v_1 \end{pmatrix} = \begin{pmatrix} e_{x0} & e_{z0} \\ \frac{e_{x0}+e_{x1}}{2} & \frac{e_{y0}+e_{z1}}{2} \end{pmatrix}^{-1} \begin{pmatrix} v_0 \\ v_1 \end{pmatrix}, \tag{19}$$

and its error variance is specified by,

$$\begin{pmatrix} \varepsilon_0^2 \\ \varepsilon_1^2 \end{pmatrix} = \begin{pmatrix} \beta_{11}^2 & \beta_{12}^2 \\ \beta_{21}^2 & \beta_{22}^2 \end{pmatrix} \begin{pmatrix} \sigma_0^2 \\ \sigma_1^2 \end{pmatrix} \tag{20}$$

where e_{xi} and e_{zi} are the components of $\boldsymbol{e}_i$. To evaluate estimation error in the vertical beam in respect to the baseline between the radar and a receiver, we set 2 parameters h and b which are the height of the target and the length of the baseline, respectively. Now we obtain $e_{x0} = 0$, $e_{z0} = 1$, $e_{x1} = -b/\sqrt{b^2 + h^2}$ and $e_{z1} = h/\sqrt{b^2 + h^2}$. Letting E represent the standard deviation of error σ_0 and σ_1, the error variance is derived by substituting them into eq. (19),

$$\varepsilon_0^2 = E^2 \tag{21}$$

$$\varepsilon_1^2 = \frac{1}{b^2}(6h^2 + 2h\sqrt{h^2 + b^2} + 5b^2)E^2.$$

References

Alcayde, D., J. Fontanari, and P. Bauer, 1982: High latitude neutral atmosphere temperature and concentration measurements from the first EISCAT incoherent scatter observations. *Ann. Geophys.*, **38**, 473–479.

Amayenc, P., J. Fontanari, and D. Alcayde, 1973: Simultaneous neutral wind and temperature oscillations near tidal periods in the *F*-region over St Santin. *J. Atmos. Terr. Phys.*, **35**, 1499–1505.

Cheong, B.L., M.W. Hoffman, R.D. Palmer, S.J. Frasier, and F.J. Lopez-Dekker, 2006: Phased

array design for biological clutter refection: simulation and experimental validation. *J. Atmos. Oceanic Technol.*, in press.

Doviak, R.J., J. Goldhirsh, and A.R. Miller, 1972: Bistatic-radar detection of high-altitude clear-air atmospheric tergets. *Radio Sci.*, **7**, 993–1003.

Fukao, S., T. Sato, T. Tsuda, S. Kato, K. Wakasugi, and T. Makihira, 1985: The MU radar with an active phased array system: 1. Antenna and power amplifier. *Radio Sci.*, **20**, 1155–1168.

———, H. Hashiguchi, M. Yamamoto, T. Tsuda, T. Nakamura, M.K. Yamamoto, T. Sato, M. Hagio, and Y. Yabugaki, 2003: Equatorial Atmosphere Radar (EAR): System description and first results. *Radio Sci.*, **38**, 1053, doi:10.1029/2002RS002767.

———, 2006: Coupling Processes in the Equatorial Atmosphere (CPEA): A Project Overview. *J. Meteor. Soc. Japan*, this issue.

Kamio, K., K. Nishimura, and T. Sato, 2004: Adaptive sidelobe control for clutter rejection of atmospheric radars. *Ann. Geophys.*, **22**, 4005–4012.

Röttger, J. and R.A. Vincent, 1978: VHF radar studies of tropospheric velocities and irregularities using spaced antenna techniques. *Geophys. Res. Lett.*, **5**, 917–920.

Woodman, R.F. and A. Guillen, 1974: Radar observation of winds and turbulence in the stratosphere and mesosphere. *J. Atmos. Sci.*, **31**, 491–505.

———, 1980: High-altitude-resolution stratospheric measurements with the Arecibo 2380-MHz radar. *Radio Sci.*, **15**, 423–430.

Wurman, J., S. Heckman, and D. Boccippio, 1993: A bistatic multiple-Doppler radar network. *J. Appl. Meteor.*, **32**, 1802–1814.

Yamamoto, M., T. Sato, P.T. May, T. Tsuda, S. Fukao, and S. Kato, 1988: Estimation error of spectral parameters of mesosphere-stratosphere-troposphere radars obtained by least squares fitting method and its lower bound. *Radio Sci.*, **23**, 1013–1021.